

# Venting and Outgassing Simulations of Pressurized Lunar Modules: Contamination of the Lunar Environment

S. Boccelli<sup>1</sup>, W.M. Farrell<sup>2,3</sup>, P. Saxena<sup>1</sup> & O.J. Tucker<sup>1,4</sup>

<sup>1</sup> NASA Goddard Space Flight Center, 8800 Greenbelt Rd, Greenbelt, MD 20771, USA

<sup>2</sup> Space Science Institute, 4765 Walnut Street, Suite B, Boulder, CO 80301, USA

<sup>3</sup> DeepSpace Technologies Inc., 8865 Stanford Boulevard, Suite 183, Columbia, MD 21045, USA

<sup>4</sup> Department of Atmospheric and Planetary Sciences, Hampton University, Hampton, VA 23668, USA

## Abstract

One objective of Artemis science is to determine the impact human activities have on the lunar environment, which might compromise science objectives and measurements. We perform a preliminary analysis of the contamination associated with airlock venting and outgassing from a prototype lunar-module geometry intended to host astronauts on the lunar surface. The air flow generated by the depressurization of the airlock, expanding in the lunar exosphere, is studied using the Direct Simulation Monte Carlo (DSMC) method for two different venting configurations and the particle flux on the surface is computed as a function of the distance from the the module. Outgassing from the main body of the module—assumed to be covered with a Multi-Layer Insulation (MLI) blanketing—and from the solar panels is then analyzed using a view-factor method, employing outgassing rates from the literature. Our results give preliminary indications of the distance at which contamination levels fall below the values characteristic of native species in the lunar atmosphere. Scientific measurements targeting  $^{40}\text{Ar}$  should be carried farther than 30–100 meters from the module, while the detection of lower-abundance species such as polar-crater water might require to travel up to and beyond 3 km from the module.

## 1 Introduction

As lunar exploration efforts increase worldwide [Schonfeld, 2023, Smith et al., 2020, Li et al., 2019, Mathavaraj and Negi, 2024, Mitrofanov et al., 2021], the need to quantify the effect of antropogenic activities on the lunar exosphere and regolith environment becomes prioritary [Killen et al., 2024a]. In-situ resource utilization (ISRU) activities [Zhang et al., 2023], deposition of chemicals from propulsion-system plumes [Farrell et al., 2022] and propellant venting procedures are contamination sources that might interfere with scientific experiments [AIII, 2020, Saxena et al., 2023] and thus require careful evaluation. As observed during the Apollo missions [Stern, 1999], water out-

gassing from spacecraft, rovers and mobile surface habitats [Kessler et al., 2022] as well as astronaut suits during Extra Vehicular Activities (EVAs) might locally exceed the exospheric volatile content [Killen et al., 2024b], preventing the succesful execution of mass-spectrometric and chemical-analyzer measurements [Cohen et al., 2024, Sultana, 2024]. Human activity is also a source of biological contamination. Airlock depressurization processes and carbon-dioxide removal sub-systems embedded in the astronaut Portable Life Support System (PLSS) [Chullen et al., 2018] are likely to expel traces of organics and bacteria on the surface [Saxena et al., 2023], interfering with astrobiological investigations [Weiss et al., 2024].

Pressurized mobile structures, serving as

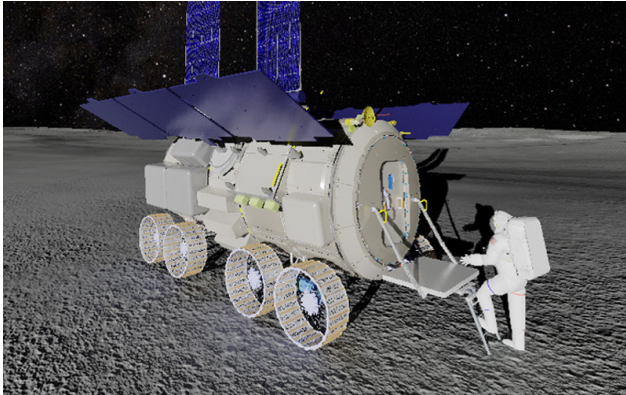


Figure 1: Artist’s rendering of the Multi-Purpose Habitation lunar module (MPH, Left) and of the Lunar Cruiser pressurized rover (Right). Credit: Thales Alenia Space / Agenzia Spaziale Italiana (ASI) [Space and ASI, 2024], and JAXA [JAXA, 2019].

habitats for astronauts, are presently being developed in support of NASA’s Artemis mission. These include the Multi-Purpose Habitation (MPH) lunar module [Illiano et al., 2024, Parodi et al., 2025], developed by the Italian Space Agency (ASI) and its prime industrial contractor Thales Alenia Space, as well as the Lunar Cruiser pressurized rover [Yamazaki et al., 2024, Yamaguchi et al., 2025] by the Japan Aerospace Exploration Agency (JAXA) and Toyota. These modules are shown in Fig. 1. Their main features include a pressurized habitation section, an airlock, and large solar panels—retracted and not visible in the Lunar Cruiser illustration of Fig. 1.

In this work we build a prototype astronaut-module geometry and perform an external gas dynamic analysis of the airlock venting process in order to characterize the possible spacial extent of surface contamination. Also, we attempt an estimation of the contamination caused by outgassing of the solar panels and of the Multi-Layer Insulation (MLI) blanketing, possibly applied on the module’s body. For this analysis we neglect important parameters such as the structure temperature, determined by the thermal design, the specific materials employed, the details on the MLI application, time on the lunar day and the exact geometry of the module. Such parameters are presently not available as the design and the definition of the ConOps are ongoing. We attempt nonetheless an order-of-

magnitude estimation based on outgassing values typical of existing spacecraft and landers [Boccelli et al., 2025].

This manuscript is organized as follows. In Section 2 we build a simplified geometry of the lunar module, inspired on available images of the future MPH. Section 3 analyzes the depressurization process using a simple zero-dimensional model. Certain pressure conditions of interest are identified from the transitory and are analyzed in detail in Section 4, where we simulate the three-dimensional expansion of the vented gas around the module and plot maps illustrating the molecular flux to the ground. In Section 5 we perform an outgassing simulation up to 120 meters from the module and in Section 6 we compare these results with the natural abundance of species to be expected on the Moon, further extending the simulated domain to a distance of 5 km. The conclusions are drawn in Section 7.

## 2 A simplified lunar-module geometry

The specific geometries of the Lunar Cruiser and of MPH are presently being defined. For the Lunar Cruiser the whole cabin vents in the lunar exosphere in preparation for EVAs [Yamazaki et al., 2024]. In case of MPH, cur-

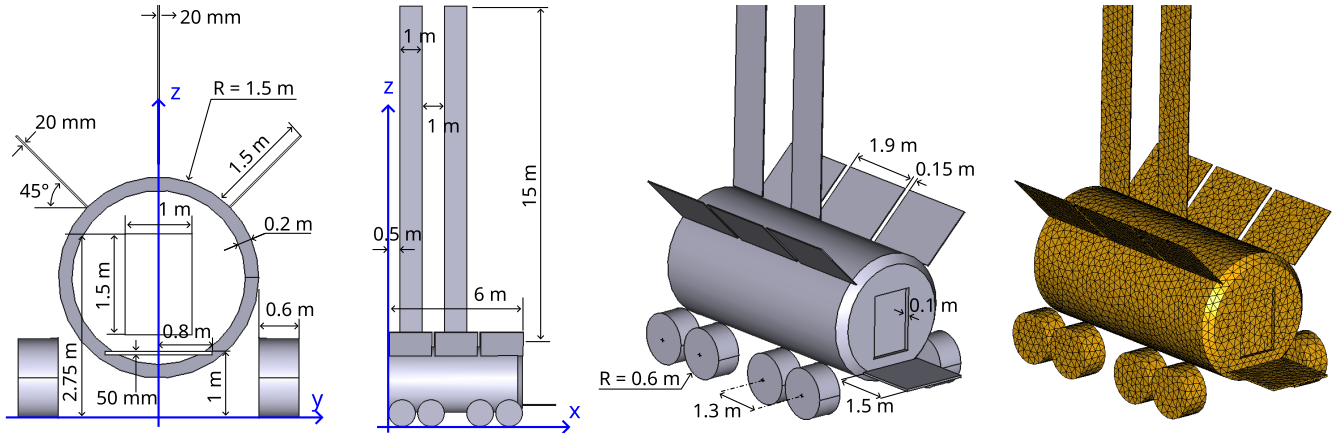


Figure 2: Simplified geometry employed in our simulations.

rent designs include a pressurized habitation module section and an airlock. Depending on energy considerations, the depressurization of the airlock might be performed by partly recycling the gas using compressors, or might be entirely vented in the exosphere. In order to simulate this venting process, we have built a simplified geometry shown in Fig. 2 and loosely based on MPH’s published images. In this geometry we take the module to have a diameter  $D = 3$  m and a total length  $L = 6$  m, divided in an habitation section ( $L_h = 4$  m) and an airlock  $L_a = 2$  m. Correspondingly, the volume of the airlock section is here approximated as  $V_a = 14.137$  m<sup>3</sup>. Our geometry includes two 15 m-long solar panels and two radiators angled at 45° with respect to the vertical plane. The solar panels and the radiators are here approximated with a thickness of 2 cm but this specific quantity is irrelevant to the simulations of this work. Figure 2-Right shows one of the surface grids employed here to compute the surface particle fluxes.

The position and orientation of the airlock venting valves is still undefined. For existing and proposed airlock designs the reader is referred to Williams et al. [2004] and Vrankar et al. [2023]. We simulate here two venting ports located symmetrically with respect to the  $(x, z)$  plane. Two different configurations are analyzed, Case 1 and Case 2, as shown in Fig. 3. In Case 1 the vents are located above the exit door and are directed horizontally. Instead, in

Case 2 the vents are directed vertically at an angle of 22.5° (that is intermediate between the vertical solar panels and the radiators, angled at 45°) and are located 0.5 m into the airlock section. The Case 1 and Case 2 configurations are simulated separately. Each vent is considered to be a circular aperture of radius  $R = 7.5$  mm as defined in Section 3.

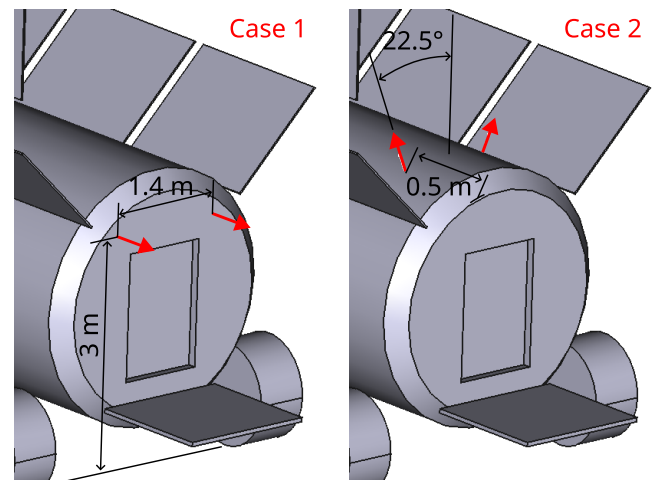


Figure 3: Position of the airlock depressurization vents for the simulations of Case 1 (Left) and Case 2 (Right).

### 3 Depressurization process: mass flow rates and vent size

In this section we estimate the outflow rates during the depressurization process and the associated vent area. These parameters are necessary to run the three-dimensional simulations of Section 4. Since MPH and the Lunar Cruiser roughly have a comparable size, our analysis can be somewhat transferred among the two different modules.

Following Parodi et al. [2025], we consider an initial gas pressure of  $P_{a0} = 56.5$  kPa, representative of the design operating pressure of the habitat section. We assume the gas is an oxygen-nitrogen mixture with an oxygen molar fraction  $X_{O_2} = 0.3$ . This satisfies the requirement that  $X_{O_2} \leq 0.37$  [Parodi et al., 2025]. The resulting mixture has an individual gas constant

$$R_i = \frac{k_B}{X_{N_2}m_{N_2} + X_{O_2}m_{O_2}} = 284.75 \frac{\text{J}}{\text{kg K}}, \quad (1)$$

where  $k_B$  is the Boltzmann constant. The equivalent (weighted) molecular mass of the mixture is  $m_{\text{mix}} = 4.85 \times 10^{-26}$  kg and the ratio of specific heats is  $\gamma = 1.4$  (only the translational and rotational modes are activated [Ferziger and Kaper, 1972]). The initial density in the airlock is thus  $\rho_{a0} = 0.6614$  kg/m<sup>3</sup>.

The evolution of  $\rho_a$  during the depressurization can be estimated from a simple zero-dimensional mass balance,

$$\frac{d\rho_a}{dt} = -\frac{\dot{m}_v}{V_a}, \quad (2)$$

where  $V_a$  is the volume of the airlock and  $\dot{m}_v = 2\rho_v u_v A_v$  is the mass flux outflowing from two circular vents, each with an area  $A_v = \pi R_v^2$ ,  $R_v$  being an effective radius for each individual valve. The gas properties at the vent are estimated here using the adiabatic expansion formulas [Liepmann and Roshko, 2001],

$$\begin{cases} T_v = T_a \left(1 + \frac{\gamma-1}{2} M_v^2\right)^{-1}, \\ \rho_v = \rho_a \left(1 + \frac{\gamma-1}{2} M_v^2\right)^{-1/(\gamma-1)}, \\ u_v = M_v \sqrt{\gamma R_i T_v}, \end{cases} \quad (3)$$

where  $M_v$  is the Mach number reached at the vent during the expansion and  $T_a$  and  $P_a$  are the temperature and pressure in the airlock. As the external pressure is negligible, near the vent the gas reaches a sonic speed (Mach number  $M_v = 1$ ). This condition completely defines the outflow velocity,  $u_v$ , and lets us compute the mass flow rate. Notice that the gas at the vent reaches  $M_v = 1$  both during the initial phases of the expansion—when the pressure is high—and also at the end of the depressurization phase, when the gas is rarefied (see for instance Sharipov [2004]).

In order to further simplify the analysis we assume that the temperature in the airlock remains constant during the depressurization and is equal to  $T_a = 300$  K. This simplifying assumption is expected to affect the specific shape of the pressure curve. However, this does not constitute an issue for the present study, since we are merely concerned with estimating reasonable values for the mass flow rates, and we are not targeting an accurate design of the depressurization process. Ultimately, since the internal temperature is held constant, the temperature at the vent also remains constant and equal to  $T_v = 250$  K throughout the expansion, and the corresponding velocity at  $M_v = 1$  is  $u_v = 315.69$  m/s.

Eq. (2) is easily solved analytically or can be integrated numerically. The depressurization curves obtained for different vent radii are shown in Fig. 4. Ultimately, depressurization curves will be designed as to meet the required dwell times for astronauts, based on health and safety requirements [Abercromby et al., 2013, Gernhardt et al., 2007]. Here, we consider only the case of a vent radius  $R_v = 10$  mm, which evacuates the airlock in about ten minutes. Other cases are analogous and this choice does not compromise the validity of the results. At  $t = 10$  min, the residual pressure in the airlock is approximately 10 Pa, which permits to effortlessly operate the outer door. The time-evolution of the mass flow rate passing through a vent with a radius  $R_v = 10$  mm is shown in Fig. 5, while the total flow leaving the airlock

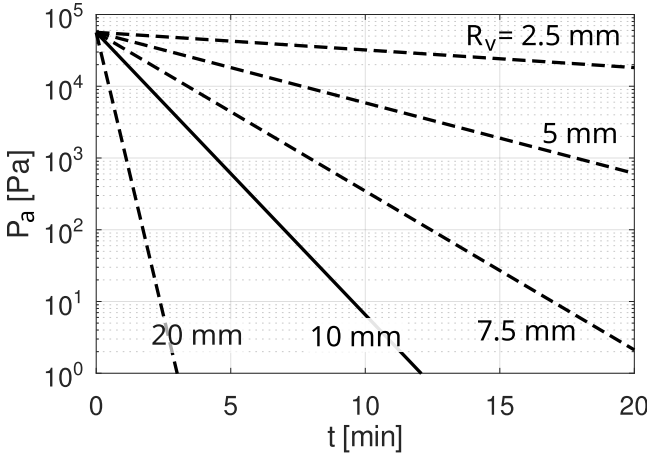


Figure 4: Airlock depressurization curves during venting from two valves each with an equivalent radius  $R_v$ . Only the case  $R_v = 10$  mm is selected in this work while the other curves (dashed lines) are not considered further.

is twice as much.

During the airlock depressurization, the density drops and the level of rarefaction of the flow through the vent increases. An order-of-magnitude indication of the importance of rarefied-gas effects can be obtained by analyzing the Knudsen number,  $\text{Kn}$ , expressing the ratio of the collision mean free path,  $\lambda$ , to the vent radius,  $R_v$ :

$$\text{Kn} = \frac{\lambda}{R_v} = \frac{1}{R_v} \frac{k_B T_v}{\sqrt{2} \sigma P_v}, \quad (4)$$

where  $\sigma$  is the elastic-collision cross-section, which can be estimated using the variable-hard-sphere parameters reported in Bird [1994] for air. At  $T = 300$  K one has  $\sigma \approx 5.5 \times 10^{-19} \text{ m}^2$ . The 30%–70% oxygen-nitrogen mixture considered here would have a similar value and a small discrepancy would not compromise our Knudsen-number analysis. The evolution of  $\text{Kn}$  at the vent is also shown in Fig. 5.

At the beginning of the depressurization, the density is sufficiently large that the collisional mean free path is small as compared to the vent radius. In this condition, the Knudsen number is approximately  $\text{Kn} \approx 10^{-5}$ , indicating that the flow is in the continuum regime and can be simulated using continuum fluid dynamic mod-

els such as the Euler or the Navier-Stokes equations [Lofthouse et al., 2007]. However, as the pressure decreases, the mean free path eventually becomes comparable with the vent size. At  $t = 10$  min the Knudsen number is  $\text{Kn} \approx 0.1$ , and the flow through the vent should be studied employing a rarefaction-capable model such as the Direct Simulation Monte Carlo (DSMC) method [Bird, 1994]. These preliminary considerations support our modeling choices discussed in Section 4.

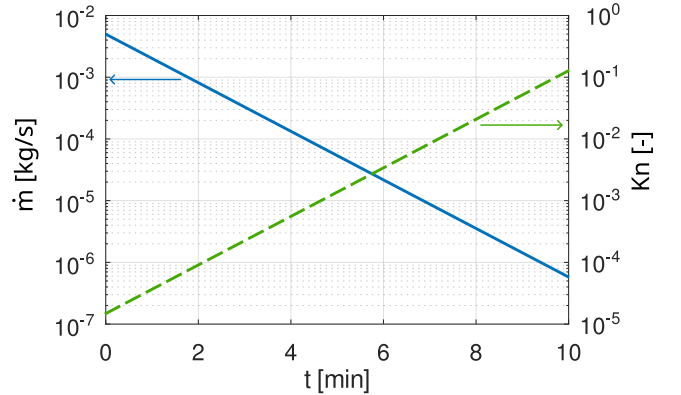


Figure 5: Evolution of the flow through a single vent of radius  $R_v = 10$  mm. Solid blue line: mass flow rate through an individual vent. Dashed green line: Knudsen number at the vent location.

## 4 Venting simulations

In order to quantify the contamination of the lunar environment associated with the airlock depressurization, we simulate the external gas expansion from a vent up to a distance of about 100 m from the module. As the gas is rarefied in the entire domain, we employ here the open-source SPARTA implementation [Plimpton et al., 2019] of the Direct Simulation Monte Carlo (DSMC) method [Bird, 1994].

As discussed in Section 3, we simulate here a mixture composed of 30%  $\text{O}_2$  and 70%  $\text{N}_2$ . We consider one single point along the depressurization curve. Specifically, with reference to Fig. 5, we select a mass flow rate (expressed through a single vent, so that the total is twice

as much) of  $\dot{m} = 5.0 \times 10^{-7}$  kg/s, corresponding to a time  $t \approx 10$  min. The gas density at the vent is  $\rho_v = 5.04 \times 10^{-6}$  kg/m<sup>3</sup> and the number density is  $n_v = 1.04 \times 10^{20}$  m<sup>-3</sup>. As mentioned, the Mach number at the vent is assumed to be  $M_v = 1$  and the temperature is  $T_v = 250$  K at any time during the depressurization process, resulting in a constant bulk velocity,  $u_v = 315.69$  m/s.

Numerically, the low pressure makes this the simplest condition of the expansion process as the gas is expected to be free-molecular in most of the external domain except at the vent, where the Knudsen number is  $\text{Kn} \approx 0.1$ . While normally this regime would be easily addressable by DSMC, the large spatial extent of the domain makes the simulations computationally demanding. In particular,

- A small time step is necessary in order to properly sample the collision rate at the vent, but it is also necessary to march in time until the particles have traveled through the large domain of interest;
- The grid needs to be refined to resolve the local mean-free-path and the vent geometry, requiring a significant number of simulated particles.

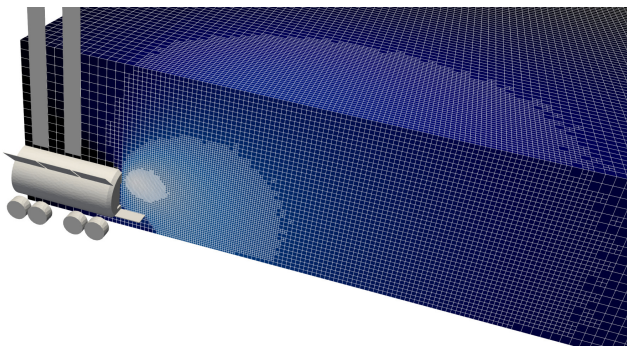


Figure 6: Detail of the computational grid employed in the front-facing vent configuration. Further refinement happens near the vent (not visible as it is embedded in the domain).

An example of the computational grid employed in this work is shown in Fig. 6. In our simulations the grid is refined based on

the number of simulated particles in each cell, which is proportional to the local mean free path. Collisions between gas molecules are modeled here using the Variable-Soft-Sphere (VSS) potential [Bird, 1994], using the parameters pre-loaded in SPARTA and reported in Table 1. Rotational relaxation happens with a variable relaxation number as discussed in Eq. (A5) of Bird [1994] evaluated with parameters also reported in Table 1.

	N <sub>2</sub>	O <sub>2</sub>
$d_{\text{ref}} \times 10^{10}$ [m]	4.07	3.96
$T_{\text{ref}}$ [K]	273.15	273.15
$\omega$	0.74	0.77
$\alpha$	1.6	1.4
$Z_{\text{rot}}^{\infty}$	18.1	16.5
$T^*$ [K]	91.5	113.5

Table 1: VSS and rotational-relaxation parameters employed in the venting simulations.

Gas-surface collisions assume a diffuse scattering (full accommodation) and the temperature of every surface is set to  $T_s = 300$  K for simplicity. The lunar regolith is simulated as a flat surface also at a uniform temperature of 300 K. The actual temperature of the lunar regolith varies dramatically based on the latitude and hour of day [Williams et al., 2017, Boccelli et al., 2026]. Additionally, shadowing caused by the body of the module, by the solar panels and the radiators could create localized low-temperature spots that might partially affect the local three-dimensional gas distribution. However, besides this effect being likely small at the considered rarefaction conditions, it also does not affect the deposition fluxes which are only defined by the source. Therefore, our simplifying choice of employing a constant surface temperature does not compromise our contamination study.

The simulations are performed as follows. We start with no particles in the computational domain, approximating the lunar vacuum. At each timestep particles are injected in the domain and a steady state is reached after about 0.6 physical seconds, with about 6 million sim-

ulated particles. At this point, in order to reduce the statistical noise of the results, we start computing running averages of the macroscopic fields to be outputted. Gravitational acceleration is neglected in these simulations because of the small size of the considered domain as compared to the ballistic spacial scales, which is in the order of tens of kilometers for air or water molecules at these temperatures.

The results of the simulations are shown in Fig. 7 in terms of density contours around the vent. Only half of the domain is shown as the simulations are symmetric. In the figure we show the local density scaled with the density at the vent, which in the present simulations is  $n_v = 1.04 \times 10^{20} \text{ m}^{-3}$ .

As the vents can be roughly interpreted as (sonic) spherical expansion points, the density is observed to drop rapidly far from them. At a distance of 1 m, the density has roughly dropped by four orders of magnitude and about five orders of magnitude at roughly 5 m. Figure 8 shows the particle flux impinging on the surfaces of the module,  $\dot{n}$  [ $1/(\text{m}^2 \text{s})$ ], normalized to the particle flux from the vent,  $\dot{n}_v$ , calculated as  $\dot{n}_v = \dot{m}/(m_{\text{mix}}\pi R^2)$ . For the simulation considered here,  $\dot{n}_v = 3.28 \times 10^{22} \text{ m}^{-2}\text{s}^{-1}$ . The results of Fig. 8 are given in dimensionless form so that one can easily re-scale them using the desired injection flow rate, obtaining an estimation for the corresponding surface fluxes.

In the figure, the normalized particle fluxes are always smaller than unity, even at the vents. This is because the plot only shows the particles *impinging* on the surface, not considering the emitted ones. At the vent location, these represent the back-scattered particles, which are roughly  $10^{-4}$  times fewer than the injected ones.

As one might expect, the front-facing venting configuration results in a larger possible contamination of the lunar surface as compared to the top-facing one. This is also reflected in Fig. 9, where we show the footprint of the contamination at a distance from the module. To aid the interpretation of the results, the particle deposition fluxes of Fig. 9-Top are extracted along lines oriented along  $x$  and  $y$  and are shown

in Fig. 9-Bottom. The results shown in Fig. 9 bottom out at  $\dot{n}/\dot{n}_v = 10^{-9}$ . This is due to the finite number of simulated particles: at these low values, either a single simulated particle hits the surface element, resulting in a scaled flux of  $10^{-9}$ , or no simulated particle hits the surface at all. Simulations with a larger domain are possible but will require to improve the statistics by either increasing the sampling time, by employing more simulated particles or by using a coarser surface grid.

### Extrapolating the results to higher-pressure conditions

In this section we have only considered a single pressure condition of the whole depressurization curve. Simulating earlier conditions directly would make the computational requirements stricter: for higher airlock pressures the vent density is higher and the Knusen number reduces as the gas approaches the continuum regime. In such cases, one might need to employ hybrid CFD-DSMC calculations [Charton et al., 2022, Vasileiadis and White, 2024] and/or to implement collision-limiter approaches [Titov and Levin, 2007]. Given the preliminary nature of this work, and considering that the geometry and specific operating conditions of these modules are still being defined, we believe it is not necessary to reach this level of detail and we are content with our preliminary calculations.

The presented results can be scaled using the vent (injection) values such that one can extrapolate them to the desired pressure conditions. The extrapolation can be done as follows:

1. The desired airlock pressure,  $P_a$ , is selected;
2. The associated time during the depressurization is obtained from the solid line in Fig. 4;
3. The mass flow rate,  $\dot{m}$ , is then found from Fig. 5;

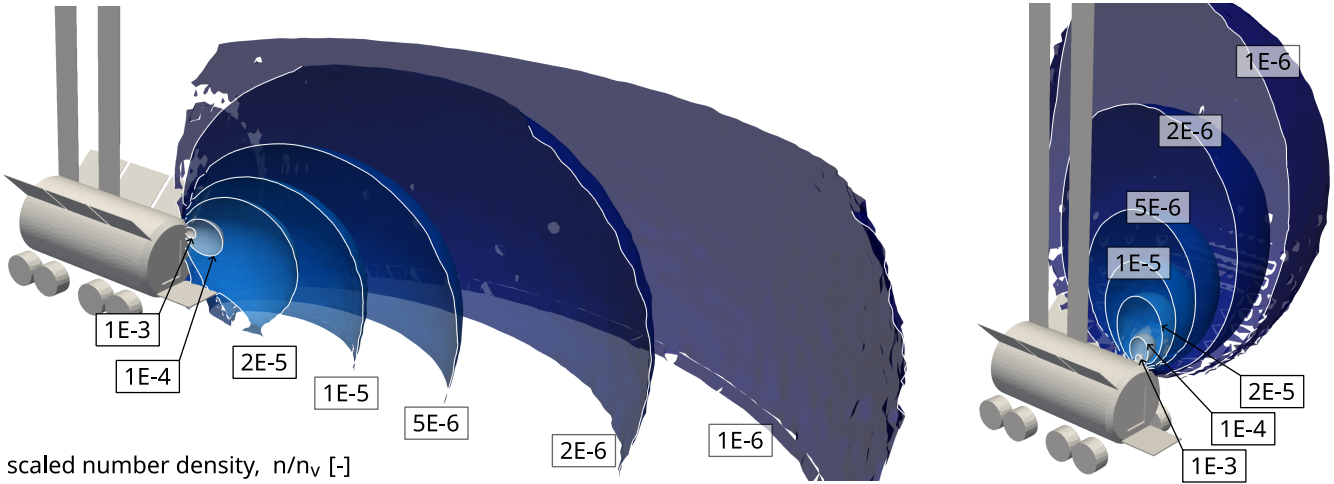


Figure 7: Contours of the number density, scaled with the vent density. Left: front-facing vent configuration. Right: top-facing vents. The plots show cuts of the simulated domain through the vent center.

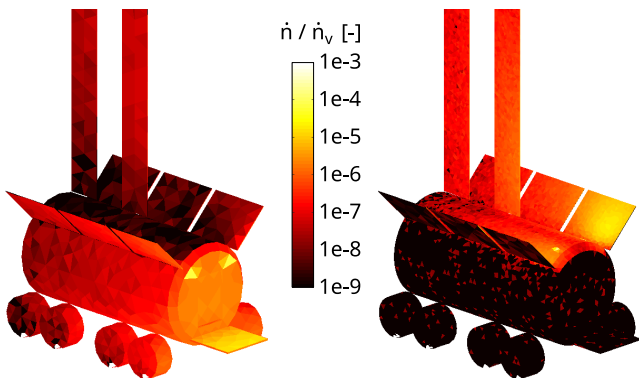


Figure 8: Incident particle flux to the module surfaces normalized with the flux injected from one vent,  $\dot{n}/\dot{n}_v$ , with  $\dot{n}_v = \dot{m}/(m_{\text{mix}}\pi R_v^2)$ . Front-facing (Left) and Top-facing vents (Right).

4. Recalling that the vent radius is  $R_v = 0.01$  m, the molecular mass of the mixture is  $m_{\text{mix}} = 4.85 \times 10^{-26}$  kg and the exit velocity is  $u_v = 315.69$  m/s throughout the expansion, one computes the vent number density ( $n_v$ ) and the particle flow rate through the vent ( $\dot{n}_v$ ) as

$$\begin{cases} n_v = \dot{m}/(m_{\text{mix}}u_v\pi R_v^2) \\ \dot{n}_v = n_v u_v \end{cases} \quad (5)$$

5. The quantities shown in Figs. 7, 8 and 9 can then be multiplied by  $n_v$  and  $\dot{n}_v$  respectively, obtaining the flow field at the desired airlock pressure.

As stated, this extrapolation is approximated, as the flow regime changes at higher pressures, but we believe that these initial estimates provide useful quantitative insights nonetheless, especially at this stage of the design process.

## 5 Outgassing simulations

Outgassing rates depend on

- The operating thermal conditions of the module (bake-off of the sunlit elements and re-deposition of volatiles on cold surfaces);

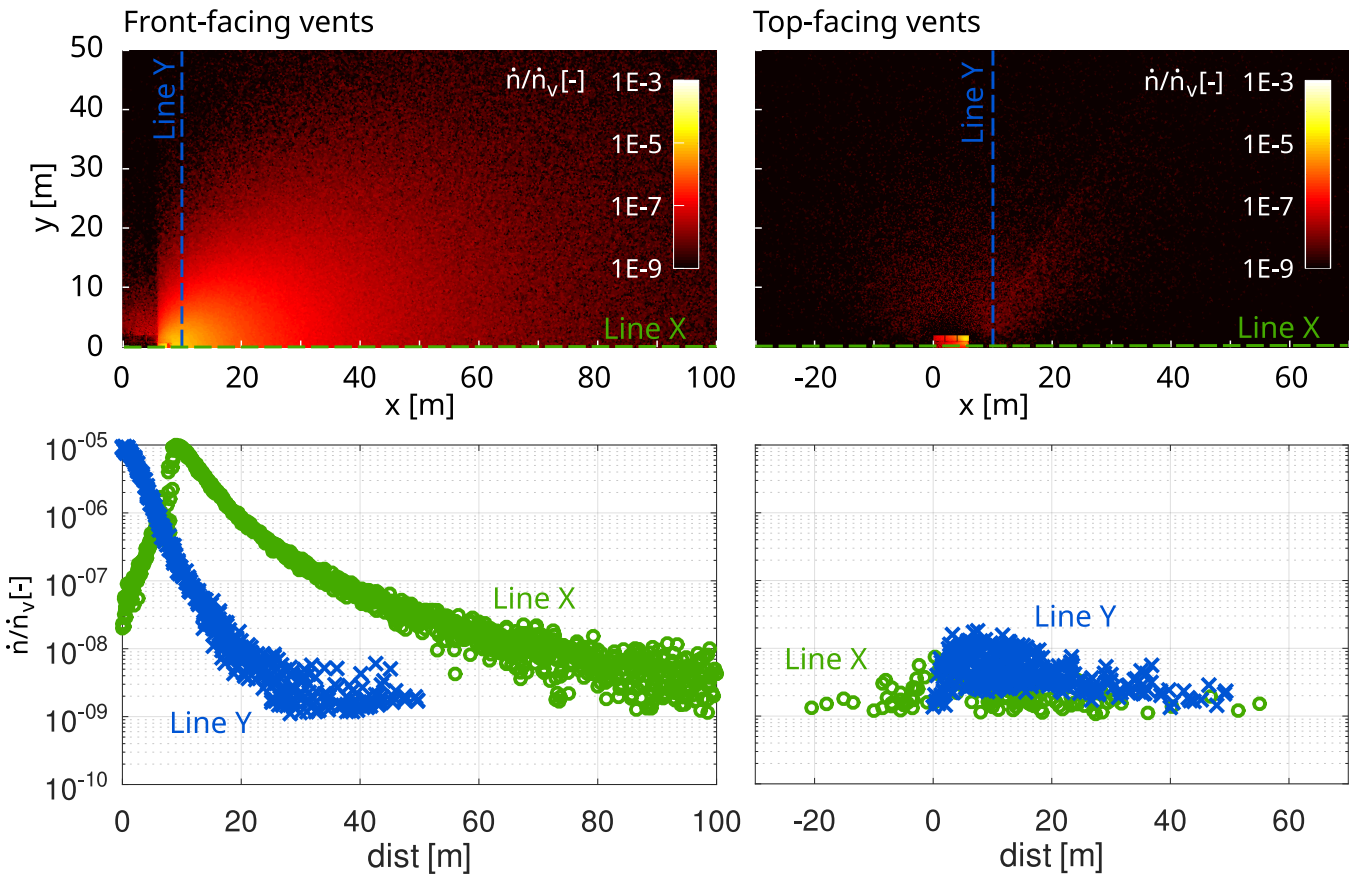


Figure 9: Top: incident particle flux at a distance from the module, normalized with the flux injected from one vent,  $n/n_v$ , with  $\dot{n}_v = \dot{m}/(m_{\text{mix}}\pi R_v^2)$ . Bottom: same values extracted along the horizontal and vertical lines shown in the Top panel. Left boxes: front-facing vents. Right boxes: top-facing vents.

- ii) The specific materials and design configuration;
- iii) The amount of time spent in space, which might span multiple lunar days;
- iv) Airlock venting operations, which deposit fresh molecules on the (shadowed or sunlit) surfaces.

At the present design stage the mentioned factors are not entirely defined, making an accurate outgassing prediction challenging. Yet, we attempt here an approximated analysis based on our simplified geometrical model.

On MPH and on the Lunar Cruiser, notable sources of outgassing molecules will include the solar panels, the payloads and external structures. The latter two will emit molecules that are eventually released into the lunar environment through venting paths in the blanketing. Additionally, the Multi-Layer Insulation (MLI) blanketing itself is a well-known outgassing source [Petro et al., 2014]. We provide here an approximated prediction based on outgassing rates measured on other spacecraft.

## Outgassing rates from the literature

Different spacecraft have been reported to show very different levels of outgassing (see for instance Fig. 10 in Boccelli et al. [2025]). Strict cleanliness and low-outgassing are typically necessary on scientific spacecraft, particularly if carrying sensitive instruments or if aimed at astrobiological investigations [Alred et al., 2020, Weiss et al., 2024]. Instead, higher levels of water pressure—attributed to outgassing—have been recently detected in the exosphere surrounding commercial spacecraft [Cohen et al., 2025]. In the case of Peregrine Mission-1, the outgassing mass flow rate, inferred from mass-spectrometric measurements, was estimated to be  $\dot{m} = 2.85 \times 10^{-8} \text{ g cm}^{-2}\text{s}^{-1}$  [Boccelli et al., 2025]. This value is comparable to that of the Space Shuttle, typically attributed to the release of atmospheric humidity absorbed in the porous heat-shield tiles and then desorbed in

space [Paterson and Frank, 1989, Killen et al., 2024b].

Measurements on the Midcourse Space eXperiment (MSX) satellite a few days into the mission suggested a water-molecule release rate—primarily attributed to the MLI—of  $3 \times 10^{-12} \text{ g cm}^{-2}\text{s}^{-1}$  (see Taylor et al. [1997] and Silver et al. [1997]). These values are analogous to those observed on the Rosetta spacecraft [Schläppi et al., 2010]. Fugett et al. [2022] also report values of roughly  $10^{-12} \text{ g cm}^{-2}\text{s}^{-1}$  for MLI under vacuum-testing conditions, and the main observed constituent species was water. It should be mentioned that these rates have been shown to increase dramatically, up to  $10^{-9} \text{ g cm}^{-2}\text{s}^{-1}$ , when the MLI was exposed to a Jupiter-like radiation environment [Fugett et al., 2022]. Testing of silicon-based materials [Soares et al., 2019], characteristic of the solar panels, also showed order-of-magnitude increases in the outgassing rates under the effect of strong radiation, starting from  $10^{-8} \text{ g cm}^{-2}\text{s}^{-1}$  during irradiation and decaying to about  $10^{-10}$  or  $10^{-11} \text{ g cm}^{-2}\text{s}^{-1}$  about 100 hours afterwards. A variety of outgassed species was detected from these materials, including organic compounds in the irradiated case. Analysis by Petro et al. [2014] for the MAVEN spacecraft suggests a solar-panel outgassing rate larger than  $4.6 \times 10^{-13} \text{ g cm}^{-2}\text{s}^{-1}$  and with an upper bound of  $10^{-10} \text{ g cm}^{-2}\text{s}^{-1}$ , which is roughly in line with the experiments of Soares et al. [2019]. Measurements performed on flown and unflown solar cells of the MIR space station [Harvey et al., 2000] also suggested levels of outgassing of  $10^{-10} \text{ g cm}^{-2}\text{s}^{-1}$ , and the detections suggested the presence of about 25 different species including silicone oils and hydrocarbons. Finally, for an analysis of various other materials employed on the International Space Station the reader is referred to Huang et al. [2016].

## Numerical simulations

In view of the mentioned literature references, we simulate here the following outgassing rates:

- The solar panels are assumed to outgas at  $\dot{m} = 10^{-10} \text{ g cm}^{-2} \text{s}^{-1}$ ;
- The cylindrical body of the module (habitat and airlock) is assumed to be entirely blanketed with MLI and outgassing at a rate of either  $\dot{m} = 3 \times 10^{-12} \text{ g cm}^{-2} \text{s}^{-1}$  (representative of MSX/Rosetta measurements) or at  $\dot{m} = 3 \times 10^{-8} \text{ g cm}^{-2} \text{s}^{-1}$  (PITMS' measurements on Peregrine Mission-1). Actual outgassing values for the future pressurized rovers are likely to be somewhere in the middle;
- For simplicity, the wheels, radiators and any other structures do not outgass and act as absorbing surfaces.

As outgassing results in very low densities, we compute the deposition particle fluxes using a collisionless view-factor model. The surfaces of the module and the regolith are discretized in triangular facets and the mass flow rates reaching each surface element is computed geometrically assuming a cosine-law emission.

Our calculations distinguish the flux from the MLI (mainly water) from that of the solar panels (mixture of various species including organic compounds). These different contributions are shown in Fig. 10. The contamination from the MLI is mostly localized near the main body and peaks right underneath it. Instead, contamination from the solar panels is maximum at a distance of roughly 10 m. This result is entirely geometrical and is due to the vertical elevation of the panels and to the shadowing caused by the radiator and by the main body.

In Fig. 11 we report the deposition fluxes as a function of the lateral distance from the module, extracted along the white dashed lines of Fig. 10. In this plot we include both the case of a low MLI outgassing rate and also the higher one. The position  $y = 0$  represents regolith points located immediately underneath the module body. At this location, the resulting deposition rates from the MLI can be seen to approach the values  $2 \times 10^{-12}$  and  $2 \times 10^{-8} \text{ g cm}^{-2} \text{s}^{-1}$  for the two simulations re-

spectively. These values coincide with the emission rate, due to the close proximity of the lunar surface to the blanketing—which constitutes an indirect verification of our numerical implementation.

An even larger simulation domain is analyzed in Section 6. However, it should be noted that the present analysis methodology cannot be spatially extended indefinitely. At much larger distances than those considered here (say, tens of kilometers) the particle trajectory is not rectilinear anymore and additional fallout can be expected due to gravity. Additionally, at such distances one might have to include other phenomena in the analysis, such as the ionization of outgassed molecules caused by solar radiation and the interaction with the solar wind plasma. Such a higher-accuracy analysis goes beyond the scope of the present work but might be necessary in the case of very strict contamination requirements, where instruments would have to be placed at large distances from man-made structures.

## 6 Natural densities in the lunar exosphere

We can compare the numerical contamination profiles in Fig. 11 with the mass flux associated with natural species in the lunar exosphere. Table 2 lists the surface-incident mass flux from some of the key exospheric species. For  $^{40}\text{Ar}$ , He, and Ne, density values from Farrell et al. [2023] are used and assume an exosphere temperature of 300 K. The mass flux of the water exosphere assumes a  $< 3 \text{ cm}^{-3}$  density upper limit derived from LADEE NMS measurements [Hodges and Farrell, 2022]. Regarding  $\text{H}_2$ , Tucker et al. [2021] found molecular density values consistent with about 20% of the incident solar wind converting to  $\text{H}_2$  densities consistent with Hurley et al. [2017]. The solar wind influx is approximately  $\approx 2 \times 10^{12} \text{ m}^{-2} \text{s}^{-1}$  at the subsolar point. In the polar regions, this value is reduced by the cosine of the solar zenith angle. At a solar zenith angle of  $80^\circ$  and as-

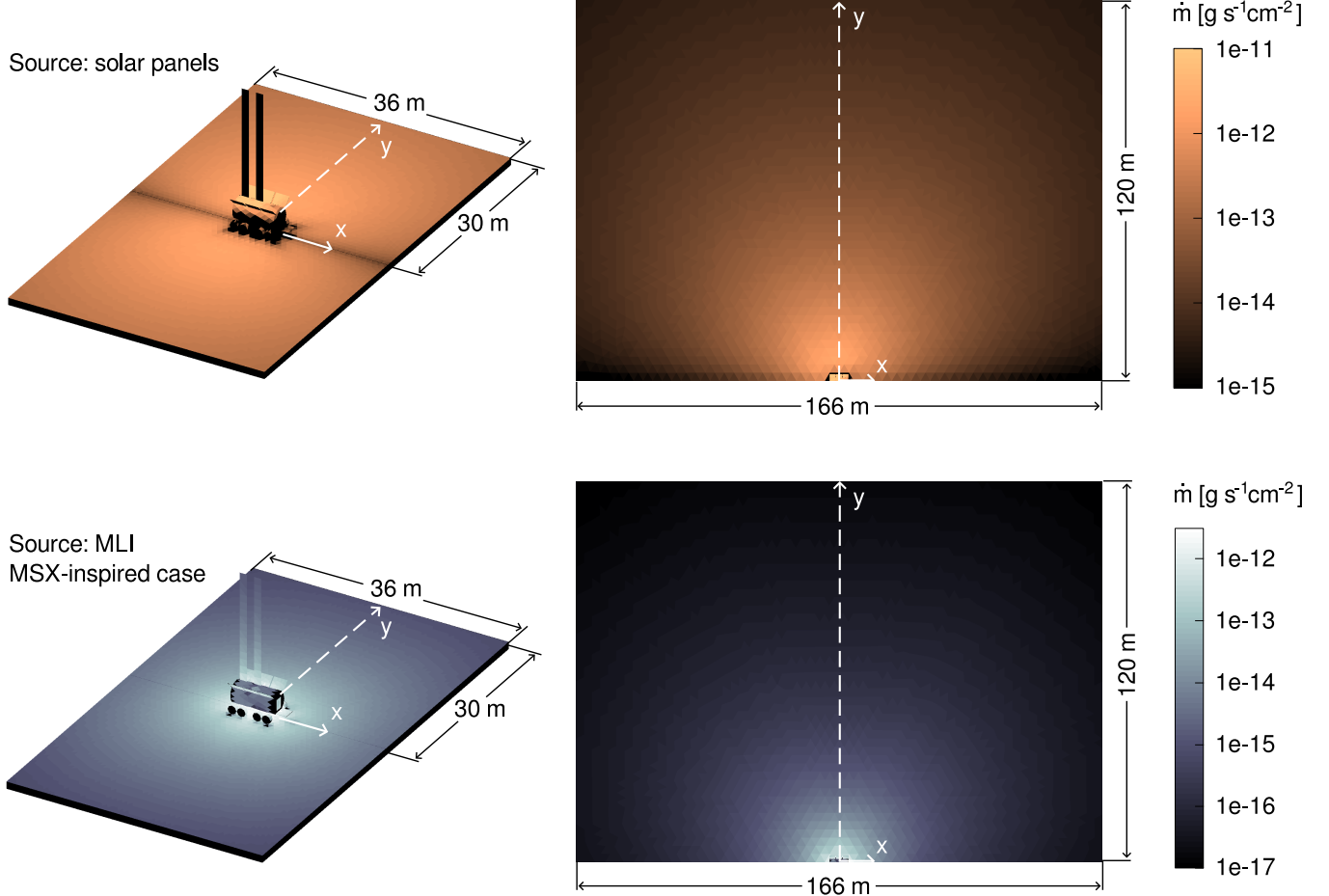


Figure 10: Outgassing simulations. Deposition rates in the vicinity of the module (Left boxes) and at a distance (Right). Top: contamination from the solar panels, emitting at  $\dot{m} = 10^{-10} \text{ g cm}^{-2} \text{ s}^{-1}$ . Bottom: contamination from the MLI for an MSX/Rosetta-like emission rate of  $\dot{m} = 3 \times 10^{-12} \text{ g cm}^{-2} \text{ s}^{-1}$ . The case of the larger MLI outgassing rate is analogous, except that the results are four orders of magnitude larger. The deposition rates extracted along the white dashed line are shown in Fig. 11.

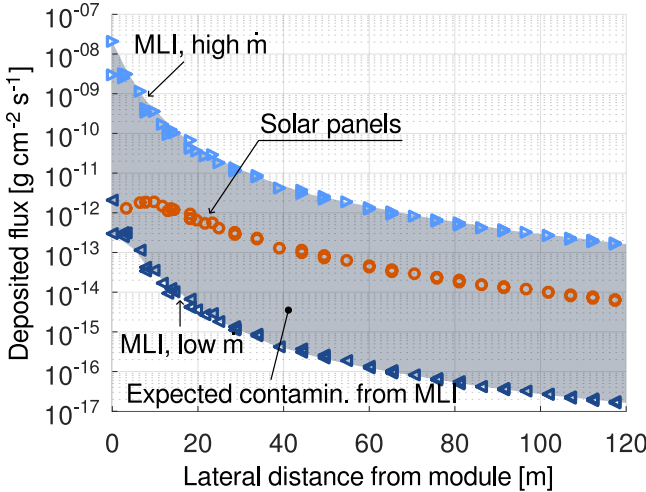


Figure 11: Lateral contamination on the lunar surface from the solar panels and the MLI (high- and low-emission scenarios). The actual contamination from MLI outgassing is expected to lie between the two simulated extremes (shaded gray region).

suming a 20% conversion efficiency, the local  $\text{H}_2$  exospheric surface mass flux would then be  $2.3 \times 10^{-17} \text{ g/cm}^2\text{s}$ .

Lunar modules might deploy at a polar region situated near a permanently shadowed crater. Therefore, in Table 2 we also include the incident mass flux from water molecules ejected from the floor of polar craters onto nearby top-side surfaces (i.e., “Polar crater water”). This polar crater water is created by impact vaporization and solar wind sputtering of a 1% icy regolith residing on the floor of a nearby polar crater (see Figure 4 in Farrell et al. [2015]). Investigators may want to place mass spectrometers or water collecting witness plates at the edge of polar craters to analyze for this floor-released water.

Most of the values of Table 2 are well below the contamination levels predicted in Fig. 11. Therefore, we have computed an additional view-factor simulation with a laterally-extended domain reaching a distance of 5 000 m. The results are shown in Fig. 12, where we also superimpose the expected mass flux of natural species. At large lateral distances,  $y$ , the deposited fluxes are expected to decay at a rate

of  $y^{-3}$ . This is due to the combined effect of (i) the spherical decay (factor  $y^{-2}$ ) and (ii) the sine of the relative angle between the emitting body and the receiving surface facet. At large values of  $y$ , where the body is low on the horizon, the sine can be approximated with a factor  $y^{-1}$ , ultimately giving the mentioned  $y^{-3}$  dependence.

Considering the worst-case scenario of high-outgassing from the MLI, the contamination levels might exceed the natural  $^{40}\text{Ar}$  and He exospheric levels within about 100 meters of the module. In such a scenario, a simple pressure gauge sensor alone, placed within that distance, would not be able to differentiate between the module’s contamination and the natural exosphere during the warm daytime. Possible solutions would be either venturing farther away from the lunar module or employing mass spectrometers. In particular, a high-resolution mass spectrometer might be able to differentiate species via mass analysis, with the natural Ar, He, and Ne exospheric species appearing as minor enhancements in associated mass channels relative to large contamination peaks at the channel associated with water and hydrocarbons. Employing species-specific high-accuracy sensors, able to measure species concentrations individually, are also a potential solution [Sultana, 2024].

For investigations targeting water molecules, operations would have to be carried further away from the lunar module. Within 120 m, the water exosphere would be “swamped” by the molecules emitted by the solar panels and by the MLI, even in the optimistic low-outgassing scenario. This distance is much larger in the case of polar crater water: investigators who may want to detect it may have to place instruments at a lateral distance of at least 3 000 m to reduce the effect of MLI contamination. Yet, even at such distances, the emission from solar panels or by abnormally-emitting MLI blanketing might remain prevalent.

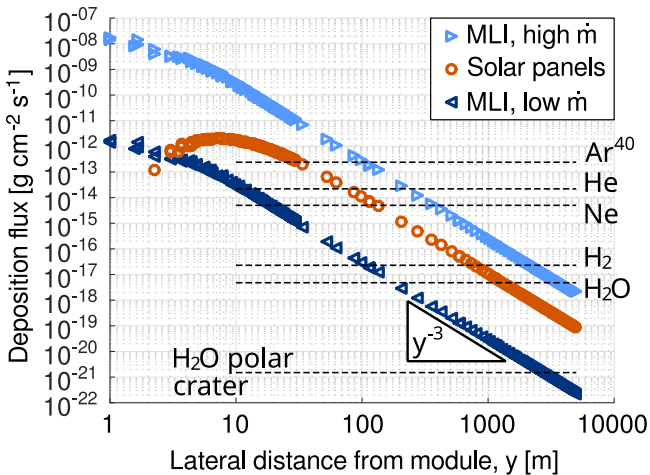


Figure 12: Deposited fluxes from the solar panels and the MLI up to 5 km from the surface module. Log scale. The triangle indicates the expected theoretical slope  $\propto y^{-3}$ . The expected natural abundance of lunar exospheric species (Table 2) is indicated with dashed lines.

Species	Mass flux [g/cm <sup>2</sup> s]
<sup>40</sup> Ar	$2.4 \times 10^{-13}$
He	$2.2 \times 10^{-14}$
Ne	$5.0 \times 10^{-15}$
H <sub>2</sub>	$2.3 \times 10^{-17}$
H <sub>2</sub> O	$< 4.8 \times 10^{-18}$
Polar crater water	$1.5 \times 10^{-21}$

Table 2: Mass flux of natural exospheric species.

## 7 Conclusions

In this work we have quantified the potential contamination of the lunar surface caused by airlock venting operations and from solar-panel and Multi-Layer Insulation (MLI) outgassing of perspective pressurized lunar modules.

After building a representative geometry, inspired from proposed mobile lunar habitat designs, we have first analyzed the depressurization process with a simplified zero-dimensional model that represents the whole airlock as a lumped volume and assumes an isentropic gas expansion through the valves. We take this simplified result as an initial condition and perform a three-dimensional Direct Simulation Monte Carlo (DSMC) analysis of the further expan-

sion of the gas into the lunar environment. This is done for two different venting geometries, either facing horizontally or vertically. The resulting self-contamination and the deposition of molecules on the lunar surface are quantified up to a distance from the module. Horizontal vents produce a particle flux on the regolith that is about 1000 times larger than the vertical-vent configuration.

Outgassing from the solar panels and from the MLI blanketing is then studied using a view-factor model. Representative values of the outgassing rates from the solar panels are taken from available literature references. For the MLI, we consider instead two limiting values: a low-emission scenario, for which we adopt the outgassing values reported in the literature for the MSX and for the Rosetta spacecraft, and a high-emission scenario, for which we employ the recent measurements performed by the PITMS mass spectrometer during the Peregrine Mission-1 (similar to those estimated for the Space Shuttle). We expect actual outgassing values for the final design of lunar modules to lie somewhere in the middle. Two-dimensional and lateral plots of the contamination are discussed.

The analysis is performed up to a distance of 5 000 m from the module and the fluxes associated with contamination are compared to the expected abundances of exospheric lunar species. Scientific investigations that involve contamination-sensitive measurements should be done at a considerable distance from the module unless special shielding design precautions are taken. Our preliminary analysis indicate that contamination might exceed the local abundance of argon atoms within a distance of 30–100 meters from the module. For other species, investigations would have to be carried farther away, and astronauts might have to venture up to and beyond 3 km to detect low-abundance species such as polar-crater wa-

## 8 Acknowledgements

The work of SB was supported by an appointment to the NPP NASA Postdoctoral Program held at NASA Goddard Space Flight Center and administered by Oak Ridge Associated Universities under contract with NASA. WMF’s work was supported by the SSERVI CLEVER grant at Georgia Tech (NNH22ZDA020C). OJT’s work was supported by the SSERVI DREAM2 and LEADER grants.

## References

Julie Schonfeld. Summary of the contracted deliveries of NASA payloads to the moon via Commercial Lunar Payload Services (CLPS). In *2023 IEEE International Conference on Systems, Man, and Cybernetics (SMC)*, pages 863–866. IEEE, 2023.

Marshall Smith, Douglas Craig, Nicole Hermann, Erin Mahoney, Jonathan Krezel, Nate McIntyre, and Kandyce Goodliff. The Artemis program: an overview of NASA’s activities to return humans to the moon. In *2020 IEEE aerospace conference*, pages 1–10. IEEE, 2020.

Chunlai Li, Chi Wang, Yong Wei, and Yangting Lin. China’s present and future lunar exploration program. *Science*, 365(6450):238–239, 2019.

S Mathavaraj and Kuldeep Negi. Chandrayaan-3 trajectory design: Injection to successful landing. *Journal of Spacecraft and Rockets*, pages 1–8, 2024.

IG Mitrofanov, LM Zelenyi, VI Tret'yakov, and DV Kalashnikov. Luna-25: The first polar mission to the moon. *Solar System Research*, 55:485–495, 2021.

Rosemary M Killen, LiHsia Yeo, Yihua Zheng, Jason McLain, John Marshall, Liam Morrissey, Caitlin Ahrens, Phillip Phipps, Heather Graham, and Timothy J Stubbs. Moon: Handle with care. *Bulletin of the American Astronomical Society*, 56(1), 2024a.

Peng Zhang, Wei Dai, Ran Niu, Guang Zhang, Guanghui Liu, Xin Liu, Zheng Bo, Zhi Wang, Haibo Zheng, Chengbao Liu, et al. Overview of the lunar in situ resource utilization techniques for future lunar missions. *Space: Science & Technology*, 3:0037, 2023.

W. M. Farrell, P. Prem, O. J. Tucker, D. M. Hurley, B. A. Cohen, and M. Benna. A lingering local exosphere created by a gas plume of a lunar lander. *Icarus*, 376: 114857, April 2022. ISSN 0019-1035. doi: 10.1016/j.icarus.2021.114857. URL <https://www.sciencedirect.com/science/article/pii/S0019103521004966>.

Artemis III Science Definition Team AIII. NASA/SP-20205009602. Technical report, National Aeronautics and Space Administration, 2020.

Prabal Saxena, Liam S. Morrissey, Rosemary M. Killen, Jason L. McLain, Li Hsia Yeo, Natalie M. Curran, Nithin S. Abraham, Heather V. Graham, Orenthal J. Tucker, Menelaos Sarantos, Aaron B. Regberg, Diane E. Pugel, Andrew W. Needham, Mark Hasegawa, and Alfred J. Wong. In Situ Optimized Substrate Witness Plates: Ground Truth for Key Processes on the Moon and Other Planets. *Earth and Space Science*, 10(9):e2023EA003004, 2023. ISSN 2333-5084. doi: 10.1029/2023EA003004. URL <https://onlinelibrary.wiley.com/doi/abs/10.1029/2023EA003004>. eprint: <https://onlinelibrary.wiley.com/doi/pdf/10.1029/2023EA003004>.

S Alan Stern. The lunar atmosphere: History, status, current problems, and context. *Reviews of Geophysics*, 37(4):453–491, 1999.

Paul Kessler, Tracie Prater, Tiffany Nickens, and Danny Harris. Artemis deep space habitation: Enabling a sustained human presence on the moon and beyond. In *2022 IEEE*

*Aerospace Conference (AERO)*, pages 01–12. IEEE, 2022.

Rosemary M. Killen, Benjamin T. Sprague, and William M. Farrell. Temporary atmospheres produced by human activities on the Moon. *Advances in Space Research*, 74(11):6158–6171, December 2024b. ISSN 0273-1177. doi: 10.1016/j.asr.2024.08.042. URL <https://www.sciencedirect.com/science/article/pii/S0273117724008615>.

Barbara A Cohen, Simeon J Barber, Phillip A Driggers, David Heather, Christopher Howe, Peter Landsberg, Thomas Morse, Roland Trautner, Feargus Abernethy, Emma-May Butroid, et al. The Peregrine Ion Trap Mass Spectrometer (PITMS) investigation development and preflight planning. *The Planetary Science Journal*, 5(9):212, 2024.

Mahmooda Sultana. From Alaska to Mars: measuring methane released from permafrost environments to understand climate feedback and habitability. In *AGU Fall Meeting Abstracts*, volume 2024, pages P33A–2866, 2024.

Cinda Chullen, Bruce Conger, Bryan Kanne, Summer McMillin, Mike Swickrath, John Fricker, and Tatsuya Arai. Swing bed scrubber design and test integration results for carbon dioxide removal in the ventilation test loop 2.0. In *International Conference on Environmental Systems*, number ICES-2018-336, 2018.

Gabriella M Weiss, Silke Asche, Hannah McLain, Angela H Chung, S Hessam M Mehr, Leroy Cronin, and Heather V Graham. Operational considerations for approximating molecular assembly by Fourier transform mass spectrometry. *Frontiers in Astronomy and Space Sciences*, 11:1485483, 2024.

Thales Alenia Space and ASI. Italy’s lunar surface habitat passes key milestone. <https://europeanspaceflight.com/italys-lunar-surface-habitat-passes-key-milestone/>. [Online; accessed 29-December-2025].

JAXA. Jaxa and toyota reach agreement on taking up the challenge of international space exploration. <https://global.jaxa.jp/press/2019/03/20190312a.html>, 2019. [Online; accessed 29-December-2025].

Simone Illiano, Raffaele Mugnuolo, Mario Musmeci, Luigi Ansalone, Federica Vagnone, Nicola Genco, Franco Fenoglio, Tiffany Nickens, and Eric Alexander. International development for lunar surface habitation. In *International Astronautical Congress 2024, Milan*, pages IAC–24,B3,1,2,x86708. IAF, 2024.

Paola Parodi, Leonardo Ricci, Jean-Pierre Musso, Simone Illiano, and Raffaele Mugnuolo. Overview of ASI Multi-Purpose Habitation (MPH) module development and ECLSS preliminary concept design. July 2025. doi: 10.32865/2346/102593.

Chiaki Yamazaki, Naofumi Ikeda, Seiji Kamiyoshi, Masaru Wada, Rieko Menjo, Hiroki Matsumoto, Junya Takeda, Norio Kimura, Yosuke Ushioda, Masaki Morinaka, et al. Overview of jaxa pressurized rover development and ecls design. 2024 International Conference on Environmental Systems, 2024.

Seiko P Yamaguchi, Tatsuya Doi, Akihito Mori, Naofumi Ikeda, and Tomoyuki Kishida. Conceptual design of the Lunar Pressurized Rover thermal control system. Prague, CH, July 2025. 2025 International Conference on Environmental Systems.

Stefano Boccelli, Orenthal J Tucker, Michael J Poston, Parvathy Prem, Tristram Warren, Aleksandra J Gawronska, Simeon J Barber, William M Farrell, and Barbara A Cohen. DSMC analysis of Astrobotic’s Peregrine Mission-1: MON-25 leak and water outgassing. *Acta Astronautica*, 2025.

David E Williams, Daniel J Leonard, Valori J Booth, and Matt Russell. International space station (iss) airlock crewlock depressurization methods. *SAE transactions*, pages 1387–1398, 2004.

Daniel Vrankar, Cyprien Verseux, and Christiane Heinicke. An airlock concept to reduce contamination risks during the human exploration of mars. *npj Microgravity*, 9(1):81, 2023.

Joel H Ferziger and Hans G Kaper. *Mathematical theory of transport processes in gases*. North-Holland Publishing, London, 1972.

Hans Wolfgang Liepmann and Anatol Roshko. *Elements of gasdynamics*. Courier Corporation, 2001.

Felix Sharipov. Numerical simulation of rarefied gas flow through a thin orifice. *Journal of Fluid Mechanics*, 518:35–60, 2004.

Andrew F Abercromby, Michael L Gernhardt, and Johnny Conkin. Fifteen-minute extravehicular activity prebreathe protocol using nasa’s exploration atmosphere (8.2 psia/34% o2). In *43rd International Conference on Environmental Systems*, page 3525, 2013.

Michael L Gernhardt, JP Dervay, D Gillis, HJ McMann, and KS Thomas. Biomedical support of us extravehicular activity. 2007.

Graeme A Bird. *Molecular gas dynamics and the direct simulation of gas flows*. Oxford university press, 1994.

Andrew J Lofthouse, Iain D Boyd, and Michael J Wright. Effects of continuum breakdown on hypersonic aerothermodynamics. *Physics of Fluids*, 19(2), 2007.

Steve J Plimpton, SG Moore, A Borner, AK Stagg, TP Koehler, JR Torczynski, and MA Gallis. Direct simulation Monte Carlo on petaflop supercomputers and beyond. *Physics of Fluids*, 31(8), 2019.

J-P Williams, DA Paige, BT Greenhagen, and E Sefton-Nash. The global surface temperatures of the moon as measured by the diviner lunar radiometer experiment. *Icarus*, 283:300–325, 2017.

Stefano Boccelli, Orenthal J Tucker, and Jessica L Noviello. A simplified ordinary differential equation for the surface temperature of airless bodies. *Earth and Space Science*, 2026.

Virgile Charton, Albert Awad, and Julien Labaune. Optimisation of a hybrid NS-DSMC methodology for continuous-rarefied jet flows. *Acta Astronautica*, 195:295–308, 2022.

Nikolaos Vasileiadis and Craig White. hybrid-DCFoam: A coupled DSMC/Navier-Stokes-Fourier solver for steady-state multiscale rarefied gas flows. *Advances in Engineering Software*, 193:103669, 2024.

Evgeny V Titov and Deborah A Levin. Extension of the DSMC method to high pressure flows. *International Journal of Computational Fluid Dynamics*, 21(9-10):351–368, 2007.

Elaine M Petro, David W Hughes, Mark S Scoundra, Philip T Chen, James R Morrissey, and Catherine A Riegle. MAVEN contamination venting and outgassing analysis. In *2014 IEEE Aerospace Conference*, pages 1–12. IEEE, 2014.

John M Alred, Maxwell G Martin, William A Hoey, Anthony T Wong, Lauren M White, Paul A Boeder, Savannah A Cofer, Adrien Dias-Ribeiro, and Carlos E Soares. Predicting terrestrial contamination of the Mars 2020 sample caching system with novel multispecies outgassing and transport models. In *Systems Contamination: Prediction, Control, and Performance 2020*, volume 11489, page 1148904. SPIE, 2020.

Barbara A Cohen, Simeon J Barber, Aleksandra J Gawronska, Feargus AJ Abernethy, Natalie M Curran, Phillip A Driggers, William M Farrell, David J Heather, Christopher Howe, Peter F Landsberg, et al. The Peregrine Ion Trap Mass Spectrometer (PITMS): Results from a CLPS-delivered mass spectrometer. *The Planetary Science Journal*, 6(1):14, 2025.

WR Paterson and LA Frank. Hot ion plasmas from the cloud of neutral gases surrounding the space shuttle. *Journal of Geophysical Research: Space Physics*, 94(A4):3721–3727, 1989.

J Taylor, D Silver, R Erlandson, P Swaminathan, M Boies, R Benson, OM Uy, GE Galica, and DFG Rault. Early-time water vapor outgassing from MSX-assessment using the DSMC method. In *35th Aerospace Sciences Meeting and Exhibit*, page 838, 1997.

David M Silver, RC Benson, Boies' MT, JS Dyer, RE Erlandson, Galica' GE, BD Green, DF Hall, JC Lesho, TE Phillips, et al. Midcourse Space Experiment molecular contamination modeling predictions for early orbital operations. In *Nineteenth Space Simulation Conference Cost Effective Testing for the 21st Century*, page 67, 1997.

Bernhard Schläppi, Kathrin Altwegg, Hans Balsiger, Myrtha Hässig, Annette Jäckel, P Wurz, B Fiethe, Martin Rubin, SA Fuselier, Jean-Jacques Berthelier, et al. Influence of spacecraft outgassing on the exploration of tenuous atmospheres with in situ mass spectrometry. *Journal of Geophysical Research: Space Physics*, 115(A12), 2010.

Daniel Fugett, Carlos Soares, Anthony Wong, John Anderson, Valentina Ricchiuti, and William Hoey. Contamination control approach to mitigating radiation induced outgassing on Europa Clipper. In *2022 IEEE Aerospace Conference (AERO)*, pages 1–9. IEEE, 2022.

Carlos E Soares, Anthony T Wong, Daniel A Fugett, William A Hoey, John M Alred, Ned W Ferraro, and Dennis O Thorbourn. High-energy radiation testing and effects on spacecraft materials outgassing. 2019.

Gale A Harvey, William H Kinard, and Linda A Wilson. Outgassing of flown and unflown Mir solar cells. In *Twenty-First Space Simulation Conference: The Future of Space Simulation Testing in the 21st Century*, 2000.

Alvin Y Huang, George N Kastanas, Leonard Kramer, Carlos E Soares, and Ronald R Mikatarian. Materials outgassing rate decay in vacuum at isothermal conditions. In *Systems Contamination: Prediction, Control, and Performance 2016*, volume 9952, pages 21–30. SPIE, 2016.

William M Farrell, Jasper S Halekas, Mihaly Horányi, Rosemary M Killen, Cesare Grava, Jamey R Szalay, Mehdi Benna, Pamela E Clark, Michael R Collier, Anthony Colaprete, et al. The dust, atmosphere, and plasma at the moon. *Reviews in Mineralogy and Geochemistry*, 89(1):563–609, 2023.

RR Hodges and WM Farrell. The arid regolith of the moon. *Geophysical Research Letters*, 49(21):e2022GL099351, 2022.

Orenthal J Tucker, William M Farrell, and Andrew R Poppe. On the effect of magnetospheric shielding on the lunar hydrogen cycle. *Journal of Geophysical Research: Planets*, 126(2):e2020JE006552, 2021.

Dana M Hurley, Jason C Cook, Kurt D Rutherford, Thomas Greathouse, G Randall Gladstone, Kathleen Mandt, Cesare Grava, David Kaufmann, Amanda Hendrix, Paul D Feldman, et al. Contributions of solar wind and micrometeoroids to molecular hydrogen in the lunar exosphere. *Icarus*, 283:31–37, 2017.

William M Farrell, DM Hurley, and MI Zimerman. Spillage of lunar polar crater volatiles onto adjacent terrains: The case for dynamic processes. *Geophysical Research Letters*, 42(9):3160–3165, 2015.